
Maria Sklodowska-Curie Actions (MSCA)
Innovative Training Networks (ITN)
H2020-MSCA-ITN-2018
Grant number 813137


**Project number 813137**

URBASIS-EU
New challenges for Urban Engineering Seismology

---

## DELIVERABLE

---

**Work Package: WP3**
**Number: D3.3 – Innovative techniques for soil-structure interaction assessment**


| | | |
|---|---|---|
| Authors: | **Skłodowska, Anna Maria** | (OGS) |
| Co-authors: | Parolai, Stefano | (OGS) |
| | Petrovic, Bojana | (OGS) |
| | Romanelli, Fabio | (UniTS) |
| Reviewer | Magrin, Andrea | (OGS) |


| | |
|---|---|
| Approval | Management Board |
| Status | Final Version |
| Dissemination level | Public |
| Delivery deadline | 30.04.2022 |
| Submission date | 30.04.2022 |
| Intranet path | https://urbasis-eu.osug.fr/Scientific-Reports-157 |

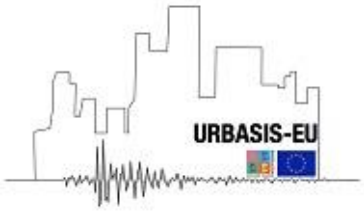

# Contents



# 1 Introduction and outline

Mitigation of the seismic risk in large urban areas is one of the challenges in engineering seismology. When in 1985 the M8.0 Michoacán earthquake caused severe destruction in Mexico City located 300 km away, the importance of the interaction between built structures and soil in case of a strong ground motion has been highlighted. Based on the Mexico City study case, Wirgin and Bard (1996) suggested that the free-field strong-motion recordings in densely urbanized areas should include the possible effects of buildings located in the neighborhood. However, even before, it was also shown that structure itself can have a significant impact on the surroundings' surface ground motion. Over 50 years ago, Jennings (1970) showed that the vibration of the Millikan Library Building can be observed at a distance up to 10 km away from the source. Since then, the development of understanding of the interaction between structures and soil was of interest to many researchers, but, still, the soil-structure interaction is generally neglected for seismic design of ordinary buildings (Fares et al., 2019).

Soil-structure interaction is a complex phenomenon and can be analyzed from many different perspectives. Kausel (2010) defined it as "an interdisciplinary field of endeavor which lies at the intersection of soil and structural mechanics, soil and structural dynamics, earthquake engineering, geophysics and geomechanics, material science, computational and numerical methods, and diverse other technical disciplines". In the same study, he stated that interactions between the structures and the soil are caused by the surface heterogeneities, such as structures themselves and their foundations. According to Chandra and Guèguen (2019), this coupling results from the stiffness impedance between the foundations and the soil, and the vibrating characteristics controlled by the dynamic properties of the structure. The energy of the coupled system vibrational response is concentrated around the frequencies of vibration of the system, which depends on the properties of the structure, soil, and foundation (Todorovska, 2009).

### 1.1 Soil-structure interaction estimation methods

Over the years, the interactions between soil-structure (SSI), site-city (SCI), and structure-soil-structure (SSSI) in engineering seismology have been extensively studied using analytical models (e.g., Paolucci, 1993; Guèguen et al., 2002) and numerical simulations (e.g., Kham et al., 2006; Liang et al., 2013; Isbiliroglu et al., 2013; Kumar and Narayan, 2017). Those studies are characterized by relatively small computation time which allows the testing influence of different parameters on SSI, however, usually they use simplified models, and validation of the results with real data is not always possible.

The other group of SSI analyses is also using data from laboratory experiments. Pitilakis et al. (2008) in addition to the numerical simulation of SSI phenomena, analyzed the problem using a shaking table facility. In other studies, Chandra and Guèguen (2019) used several centrifuge setups for analyzing how the SSI may influence the nonlinear free-field response of the soil and they compared it with frequency and time-domain methods. Similar to the numerical simulations, analyses based on laboratory experiments allow testing different scenarios with relatively low cost, yet they still have the limitations of simplified models and the scaling aspects.

The possibility of overcoming the mentioned limitations lies in the SSI analysis using real data. In two passive experiments carried out at the European Volvi test site, where a scaled building has been constructed, Guèguen and Bard (2005) analyzed the SSI using earthquake recordings and controlled explosions in the vicinity of the structure. They showed that the wavefield radiated into the ground via the foundation and coming from the vibration of the building is significant and does contaminate the so-called free-field motion. Using seismic noise, Parolai et al. (2005) analyzed the Holweide Hospital in Cologne, Germany, to investigate whether its frequencies of vibration fall into the range where soil amplification is expected. In another study, Massa et al. (2010), after studying the dynamic characterization of buildings, compared the influence of the structure's vibration on the measurements performed nearby. They concluded that in the case when both foundations and the nearby sensors are placed on a rock, the structure seems not able to produce a significant variation in the seismic response of the site. However, in the case of alluvial deposits subsoil, they observed the contribution of the free oscillations of the buildings. Recently, Petrovic and Parolai (2016) and Petrovic et al. (2018) studied strong-motion data registered by vertical arrays of sensors installed both in the buildings and nearby boreholes and showed that a significant amount of energy is radiated back from the structure to the ground.

### 1.2 Knowledge gap

The importance of polarization in data analysis has been underlined since Vidale (1986), however, so far, it gained limited attention in terms of the SSI assessment, even though it has the potential to provide important information on the nature of the analyzed waves. Because of the influence of the incident wavefield on the recorded motion, in the case of the Jalapa building in Mexico City, Cardenas et al. (2000) concluded that the polarization analysis of the wavefield radiated from the structure to the ground does not provide clear results. The SSI assessment is still a subject that requires a lot of research to be understood better, and, especially, the joint analysis of data from the structure and its surroundings with a focus on polarization analysis has the potential to fill up the existing gap in the SSI knowledge.

Within the URBASIS project, the work of ESR 3.2 is focused on the development of a new approach for data analysis for soil-structure interaction assessment from a wave propagation point of view with a special focus on polarization analysis. This Deliverable aims at presenting the progress of the development of a new approach for extracting and accounting for soil-structure interaction assessment. The structure of the deliverable is the following: the first part after the introduction (Section 2) is focused on the presentation of the developed new approach with a detailed explanation of every step used for the data analysis. In Section 3, firstly the description of the Matera experiment and the collected data are introduced. It is followed by the presentation of the results of the data analysis with the proposed approach. Finally, the concluding remarks along with planned further development of the proposed method are presented.

## 2 Proposed approach

The approach proposed for SSI assessment is a combination of the joint deconvolution (based on Petrovic and Parolai (2016)) and the polarization analysis (e.g., Pinnegar, 2006; Yoshida and Sasatani, 2008). It consists of 4 major steps which are described in the following. A general scheme of the approach is presented in Figure 1. Before the data analysis, the mean and trend should be removed from the recordings. Additionally, if the data was recorded by different types of instruments in the experiment setup, it is necessary to remove instrumental response, to analyze jointly the data.

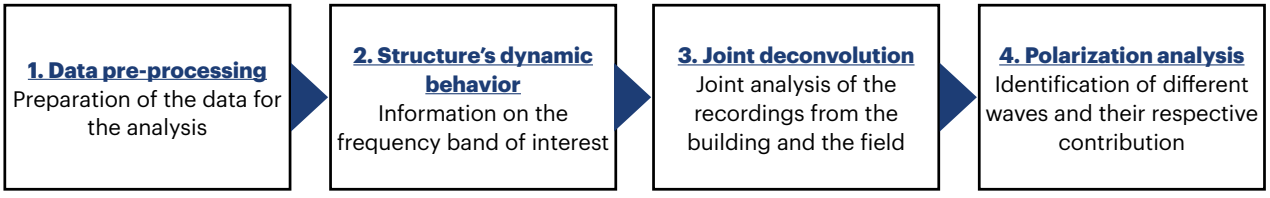


**Figure 1:** The general scheme of the major steps of the proposed approach.

### 2.1 Building dynamic behavior estimation

Estimation of the resonance frequencies of the building provides useful information for identifying the frequency range in which possible interaction might occur between the building and the soil. Since the frequency content of the wavefield radiated from the structure to the ground is expected to be

dominated by the resonance frequencies (Petrovic and Parolai, 2016), it is necessary to estimate the frequency band of interest for the following steps. As described by Snieder (2009), the motion of a structure is a combination of the excitation of the building by an earthquake from below, the coupling of the building to the subsurface, and the mechanical properties of the building. The spectral ratio method (SR), is based on the division of the Fourier spectra of the recordings registered by sensors at the top of the building by those at the bottom for the same components. SR provides the transfer function of the analyzed structure, and, therefore, information about its resonance frequencies (e.g., Paolucci, 1993; Guèguen and Bard, 2005; Snieder, 2009). This method was used in many studies for obtaining reliable results for resonance frequencies estimation (e.g., Guèguen and Bard, 2005; Parolai et al., 2005; Skłodowska et al., 2021). SR method is considered sufficient for the evaluation of the frequency range in which the possible interaction might be expected (Parolai et al., 2005).

### 2.2 Joint deconvolution of building and free field data

To evaluate the propagation from the building to its surroundings characterized by a band-limited transfer function, the earthquake data is filtered around the frequency range estimated in 2.1. Then, the recordings of the sensors installed in the building and on the soil are analyzed jointly using deconvolution (Petrovic and Parolai, 2016). Similar to the noise analysis by Petrovic et al. (2019), the method is extended to the earthquake recordings collected by the sensors installed both in the building and its surroundings. It allows the estimation of the interactions between soil and the structure based on the study of wave propagation near the surface. In the frequency domain, deconvolution is defined as:

$$S(\omega) = \frac{u(z_1, \omega)}{u(z_2, \omega)} \tag{1}$$

where $u(z_1, \omega)$ and $u(z_2, \omega)$ are Fourier transforms of the recordings at locations $z_1$ and $z_2$, respectively. In order to limit the gain of the deconvolution regions where the seismograms contain little or no information, the regularization technique based on Clayton and Wiggins (1976) is used:

$$S(\omega) = \frac{u_1(z_1, \omega) u_2^*(z_2, \omega)}{|u_2(z_2, \omega)|^2 + \varepsilon} \tag{2}$$

where the asterisk indicates complex conjugate and $\varepsilon$ is the regularization parameter referring to constant added to the denominator. $\varepsilon$ is defined as a percentage of the average spectral power. The inverse Fourier transform of the transfer function $S(\omega)$ is defining the deconvolved wavefield. In the proposed approach for recordings of sensors installed both in the building and surroundings, the station at the top of the building is used as a reference station (i.e. $u(z_2, \omega)$ in equation 1) for the joint deconvolution.

### 2.3 Seismic phases identification

In the proposed approach, the identification of the seismic phases related to the energy transmitted from the building to the ground is necessary for the further analysis of the data. Since the deconvolved wavefield in the surroundings of a structure might be very complex and contain a lot of different waves originating from different sources other than the analyzed building, in many cases the development of an analytical model of the building and considered surroundings is needed to facilitate the interpretation. The model is based on a simplified geometry and, in the case of an analyzed earthquake with sufficient epicentral distance, the assumption of a vertically propagating plane wave as input is

made. The model allows defining the transfer function for the earthquake recordings in the field with the virtual input signal at the top of the building.

### 2.4 Polarization analysis

The final step is the polarization analysis of the signal corresponding to the identified phases related to the energy transmitted from the building to the ground. It is composed of two independent analyses. The first part, aiming at polarization analysis of the deconvolved wavefield, is based on the method proposed by Pinnegar (2006) where the three-component signal can be thought of as a superposition of ellipses. Therefore, the analyzed signal can be expressed as Fourier spectra of the elements of these ellipses, i.e.:

- $a$ - the semi-major axis of the ellipse ($a \geq 0$),
- $b$ - the semi-minor axis of the ellipse ($a \geq b \geq 0$),
- $I$ - the inclination of the ellipse to the horizontal plane ($0 < I < \pi$),
- $\Omega$ - the azimuth of the ascending mode ($-\pi < \Omega < \pi$),
- $\omega$ - the angle between the ascending node and the position of maximum displacement ($0 < \omega < \pi$),
- $\phi$ - the phase, measured with respect to the time of maximum displacement ($-\pi < \phi < \pi$).

The visual representation of the ellipse elements is presented in Figure 2. Pinnegar (2006), used the S-transforms (Stockwell et al., 1996) of all three components to obtain the time-frequency spectra of the elliptical elements. Since using S-transform allows studying the polarization for each frequency separately, this method is particularly useful for cases where the analyzed signal is expected to be narrowly banded. In particular, the semi-minor axis and the difference between semi-major and semi-minor axes define the spectrum of the "circular" and "linear" parts of the ellipse, respectively. The total power S-spectrum of the polarization ellipse is defined by $\sqrt{a^2 + b^2}$ and gives an estimate of the energy density that takes all three orthogonal components of the signal into account (more detailed information on elliptical parameters and how to calculate them can be found in Pinnegar (2006)). The polarization analysis of the deconvolved wavefield in the surroundings of the building in the proposed approach is based on the evaluation of the three ellipse parameters: semi-major and semi-minor axes, and their difference, since they are defining the shape of the ellipse. The total power S-spectrum is used for focusing the study on the energy density of interest.

The second part of the polarization analysis is based on the evaluation of the particle motion of the part of the wavefield radiated from the building into its surroundings. For this purpose, we apply the approach proposed by Bindi et al. (2010) for the reconstruction of the seismic input related only to the selected phases to the deconvolved wavefield in the field. By convolving the spectra of the selected peaks from the joint deconvolution with the signal recorded on the top of the analyzed building, it is possible to reconstruct the ground motion in the field related to this particular phase (similar to Petrovic and Parolai (2016)). The reconstructed signal is later decomposed into three planes: radial (X-Z), transverse (Y-Z), and horizontal (X-Y). The estimated decomposed particle motion provides information about the polarization of the signal radiated from the building into its surroundings.

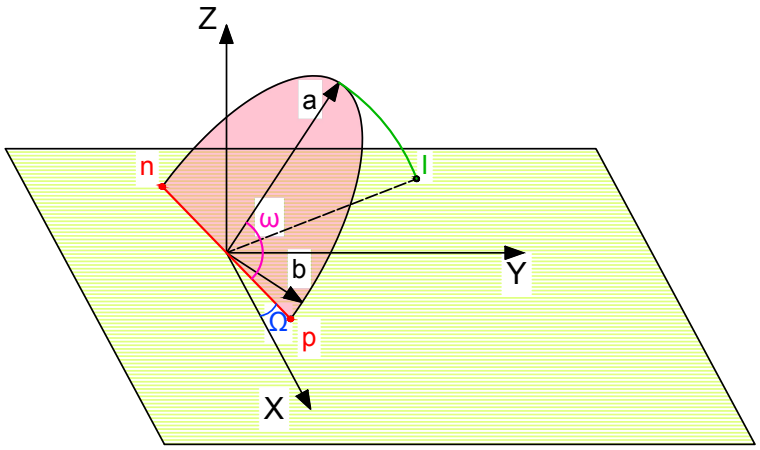


**Figure 2:** Graphic representation of the ellipse parameters. $a$ and $b$ are semi-major and semi-minor axes; $\Omega$ is the azimuth of the ascending mode; $\omega$ is the angle between the ascending node and the position of maximum displacement; $I$ is the inclination of the ellipse to the horizontal plane. $n$ and $p$ are the nodes indicating the intersection of the ellipse with the horizontal plane.

# 3 Application to a test site

## 3.1 Matera experiment

### 3.1.1 Site geology

The data used in the presented study was collected during the SSI experiment performed in Matera city in the South of Italy (Figure 3) in October 2019. The subsoil of the test site area is consisting, starting from the top, of thin layers of yellow and red sands overlaying sub-appennine clays, and below Gravina calcarenites and Altamura limestone (Gallipoli and Lupo, 2012; CLARA project, 2020). The average shear wave velocities of the mentioned soil layers estimated by Gallipoli and Lupo (2012) are presented in Table 1. The resonance frequency of the soil in the studied area is approximately 1.6 Hz (CLARA project, 2020).

| Soil type | S-wave velocity [m/s] |
|---|---|
| Sand | 250 |
| Subappennine clay | 367 |
| Garvina calcarenite | 914 |
| Altamura limestone | 1052 |

**Table 1:** The average shear wave velocities of the soil layers in Matera.

### 3.1.2 Building description

The building instrumented in the Matera experiment is a 30 m heigh 7-floor reinforcement concrete building composed of three very similar building units connected with joints. The analyzed building has different dimensions in two main directions: the longer side of the building (later called Y) is around 69 m long (3 x 23 m) and the transverse side (shorter one, later X) is around 12 m long.

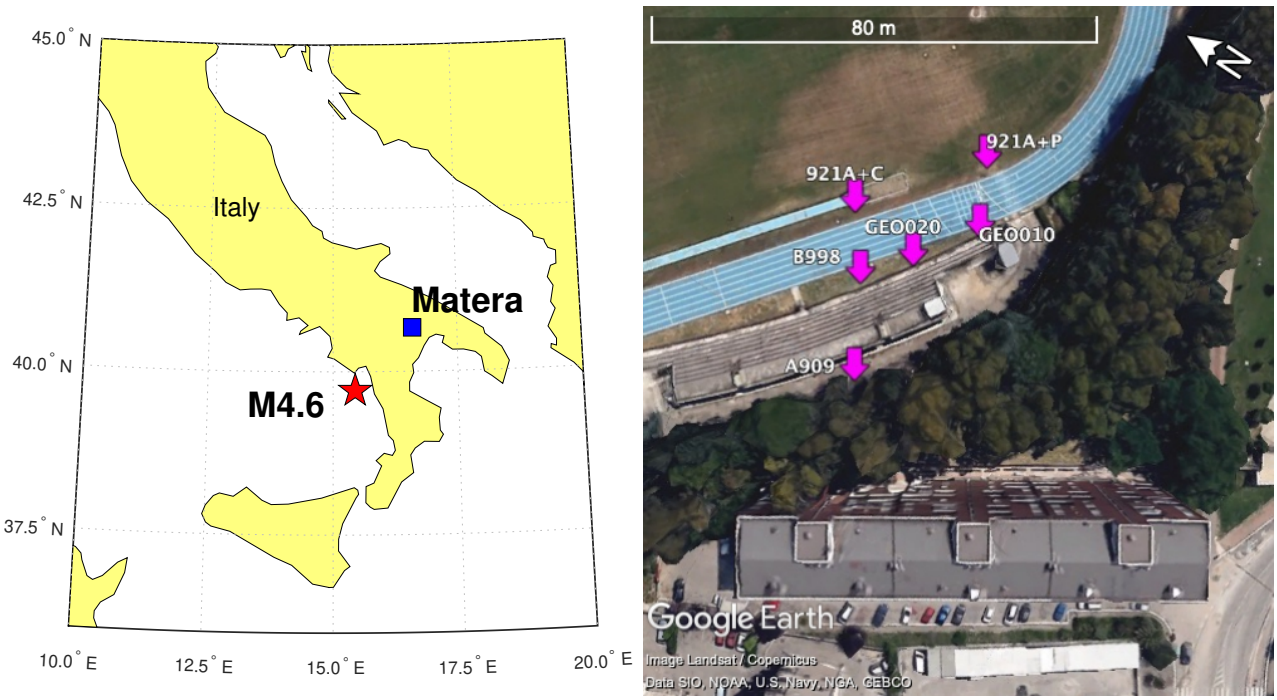


**Figure 3:** Left: Location of the Matera city in Italy (blue rectangle) and the epicenter of an M4.6 Catanzaro earthquake recorded during the experiment on 25.10.2019 (red star). Right: The experiment site with indicated location of the sensors installed in the athletic field (pink arrows).

### 3.1.3 Sensors description

During the experiment, a dense array of sensors was installed both in the building and on the nearby athletic field. There were two sensor setups (Figure 4): the first aiming at the soil-structure interaction analysis, and the second - at a better understanding of the structure's dynamic behavior. The experiment's instrumentation consisted of three types of three-component velocitimeters: CUBE connected to LE-3Dlite 1s with a sampling rate of 200 Hz, and Reftek connected to LE-3Dlite 1s and Lunitek Sentinel Geo, both with a sampling rate of 250 Hz.

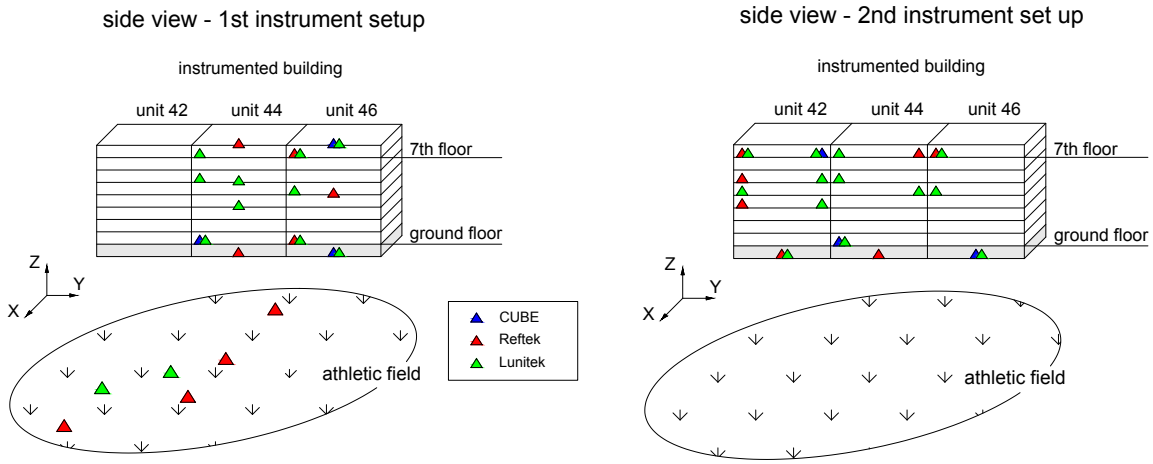


**Figure 4:** Total instrumentation and their location in the building and on the athletic field during the Matera experiment. CUBE connected to LE-3Dlite 1s sensors are marked with dark blue triangles, Reftek connected to LE-3Dlite 1s sensors - with red triangles and Lunitek Sentinel Geo - with green triangles. Left: 1st instrumental setup for SSI assessment, right: 2nd setup for better building dynamic behavior analysis.

For the first three days of the experiment, two out of three building units (44 and 46) were instrumented with three-component velocimeters located on different floors in stairwells and some of the apartments (depending on availability), and in the athletic field.

In some locations in the building, two different types of sensors were installed next to each other to double-check their performance. In the case of doubled data in the location of one sensor, only the data from CUBE or Reftek was analyzed. Since Lunitek sensors' were used for testing the instruments, recordings from those instruments were not taken under consideration for the later analyses. In the second instrument setup, some senors were moved to the right side of unit 44 and in the apartments of unit 42 which previously were not instrumented (Figure 4 right). This part of the experiment aimed to better understand the structure's dynamic, and, especially, the behavior of the joints between the units.

For the analysis of the data with the proposed approach, two sensors' sub-arrays called Array 1 and Array 2 were extracted - indicated in Figure 5 with blue and orange colors, respectively. Array 1 in unit 46 consisted of three sensors installed in the stairwell and two sensors, around 20 and 60 m from the building, installed in the field in line with the building's vertical array. Array 2 consisted of four sensors installed in the stairwell of unit 44 and one sensor in the field, around 60 m from the building.

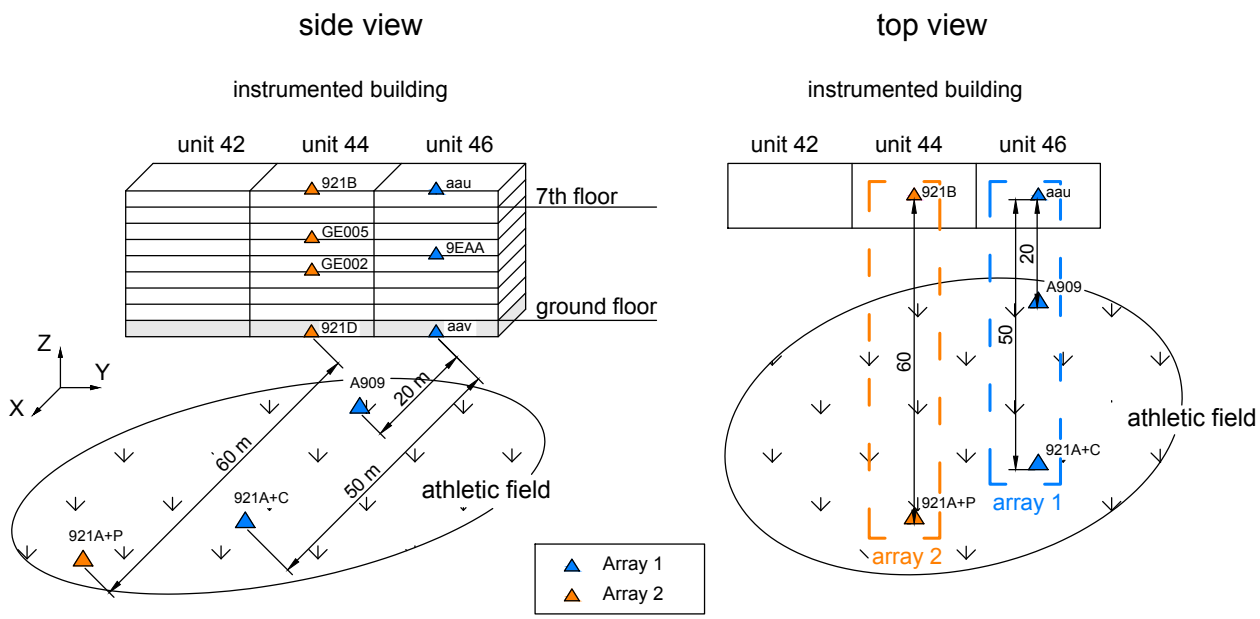


**Figure 5:** Location of the sensors in Array 1 (blue triangles) and Array 2 (orange triangles) in the building and on the athletic field. Left: side view, right: top view

### 3.1.4 Measurements/data description

During five consecutive days (22-26.10.2019) different data acquisition was performed. The main idea for the experiment was to record seismic noise, however, by chance, one earthquake M4.6 (EQ) was recorded. The epicentral distance of the registered event was around 145 km from the test site and it is marked on the map in Figure 3 with a red star.

In this study, the seismic noise data was used only for the evaluation of the building's dynamic behavior. The occurrence of the earthquake during the acquisition provided useful data for the testing of the proposed approach. For joint deconvolution and polarization analysis, only the EQ recordings registered by the sensors in two indicated sub-arrays were considered (Figure 5). For all of the calculations, the sampling rate of all of the recordings was set to 200 Hz.

## 3.2 Results from the analysis

### 3.2.1 Building's dynamic behavior

Using the noise recordings from all of the available vertical arrays in all three units from both setups, the spectral ratios were calculated to evaluate the building's dynamic characteristics. The smoothed noise SRs for each vertical array are presented in Figure 6. In the X direction, the first peak is at 2.5 Hz in all considered arrays. Interestingly, the second peak at 2.7 Hz changes amplitude depending on the array location and it is most significant in the arrays at the edge of the building. Moving towards the center, the 2.7 Hz peak is slowly decreasing to completely disappear in the middle of the building (unit 44 middle). The third peak at 3.9 Hz in the X direction has a smaller amplitude but it is shown by all the calculated SRs. The shape of the SRs in the Y direction has less variation connected to the location of the array than it is observed in the X direction. The two main peaks in the Y component are very close at 2.5 Hz and 2.7 Hz and are present in all the SRs. The third peak at 3.9 Hz is only present in the SRs in the external units. In the Z component, there is no clear amplification of frequencies.

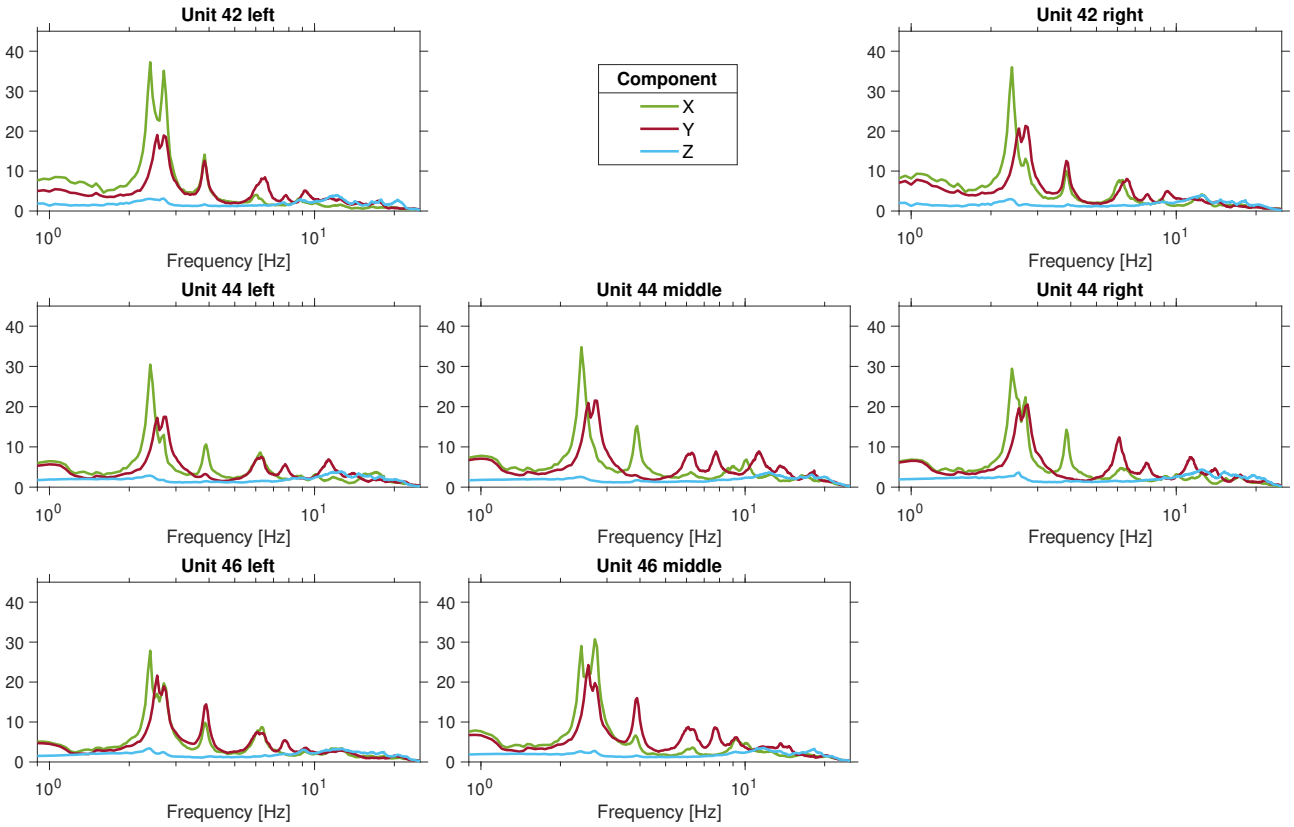


**Figure 6:** Spectral ratio for each vertical array in the building. The green line - X component, the red line - Y component, the blue line - Z component

For four vertical arrays in the building, it was possible to perform SR using also EQ data. The

comparison of the EQ and noise SRs is depicted in Figure 7. Based on the obtained results, the variation of the resonance frequencies during the shaking observed in other studies (e.g, Guéguen and Colombi, 2016; Astorga et al., 2018; Skłodowska et al., 2021) is not significant in the analyzed case. However, the shape of the spectra differs for each input. The most significant differences are observed in the SRs for the X component, however, despite those variations, most of the vibration energy of both horizontal components is distributed around 2 Hz and 10 Hz, therefore those cut-off frequencies were used for bandpass filtering of the data in further analysis.

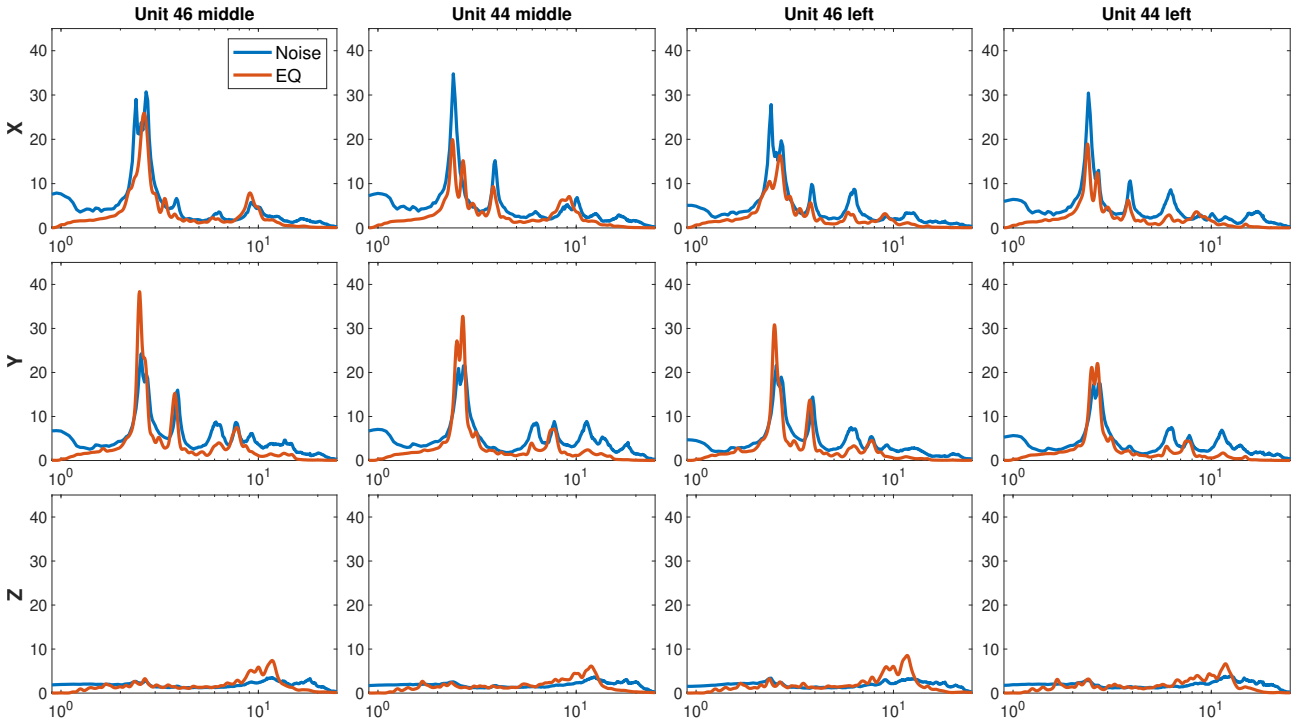


**Figure 7:** Comparison of noise (blue) and EQ (orange) spectral ratios for each component

### 3.3 Joint deconvolution

The results of the joint deconvolution of the EQ recordings in the time domain of all of the sensors in each array are shown in Figures 8 and 9, for Array 1 and Array 2, respectively. For the presented calculation, each of the sensors in an array was deconvolved using the sensor at the top of the building as a reference. The blue dashed lines on the time plots indicate the time delays of the acausal peaks of the sensors at the bottom of the building (aav for Array 1 and 921D for Array 2). In this study, $\varepsilon$ was set to 1 % of the average spectral power of $u_2$.

The deconvolved wavefield in the building (aau, 9EAA, and aav in Array 1 and 921B, GE005, GE002, and 921D in Array 2) shows expected symmetrical behavior in the causal and acausal part which can be related to the up and down-propagating waves in the structure. A small decrease of the amplitudes in the causal compared to the acausal part is due to the loss of energy in the structure (Snieder and Şafak, 2006). The deconvolved traces of the sensors installed in the field (A909 and 921A+C in Array 1 and 921A+P in Array 2) do not have symmetrical behavior as it is observed in the building and the peaks in both arrays in the acausal part are arriving after the one at the bottom of the building (blue dashed lines).

For the vertical component (Z), the separation of the acausal and causal phases is not visible due to the

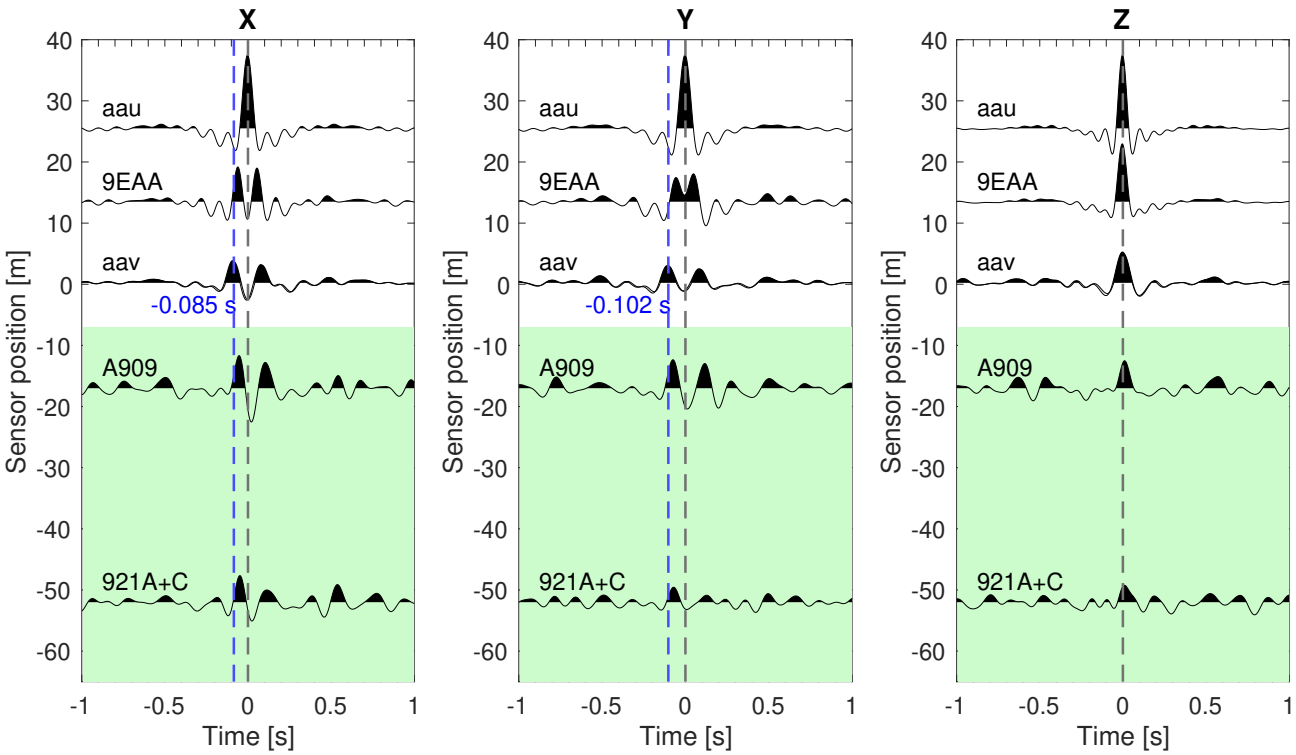


**Figure 8:** Deconvolution results Array 1. Gray dashed lines indicate a 0-time delay. Blue dashed lines in two horizontal component plots indicate the time delays of the acausal peaks of the sensors at the bottom of the building. The green background indicates sensors installed on the athletic field.

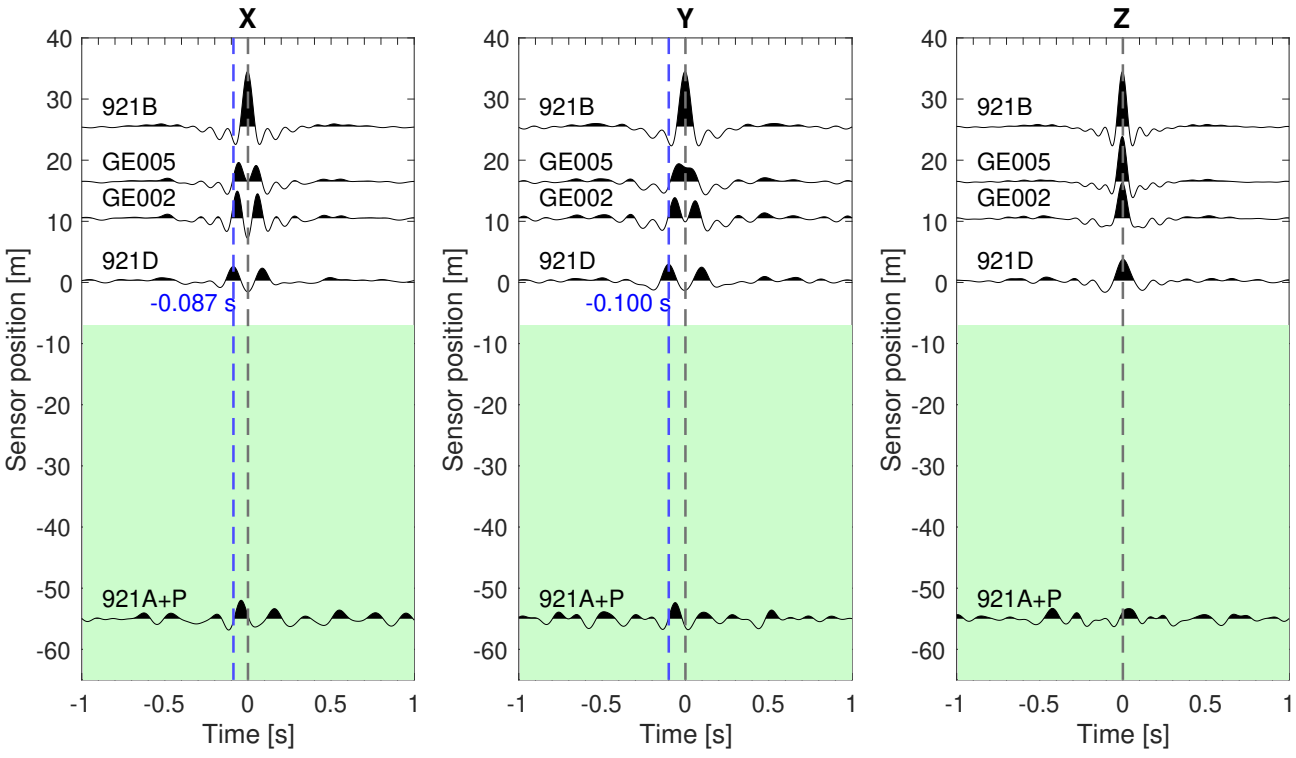


**Figure 9:** The same as Figure 8 but for Array 2.

much higher wave propagation velocity in this direction. Some peak separation is visible in the traces at the biggest distance from the building (senors 921A+C and 921A+P), however, the resolution of the deconvolution results is not sufficient enough for proper identification.

### 3.4 Phases identification

To better identify and interpret the phases of the deconvolved wavefield, and especially the phases related to the wavefield transmitted by the building to the ground, an analytical model was developed. The model is based on the simplified geometry (Figure 10) and assumption of the input, $x_0(t)$, as a vertically propagating plane wave and it defines the transfer function for the earthquake recordings in the field, $x(t)$, with the virtual input signal at the top of the building $y(t)$. In the Fourier domain, it is defined as:

$$\frac{X(\omega)}{Y(\omega)} = \frac{1}{1+r}e^{-i2\pi f(-\tau_1+\tau_3)} + \frac{r}{1+r}e^{-i2\pi f(\tau_1+\tau_3)} + \frac{(1-r)}{2}e^{-i2\pi f(\tau_1+\tau_2+\tau_3)} \tag{3}$$

where $X(\omega)$ and $Y(\omega)$ are Fourier transforms of $x(t)$ and $y(t)$, respectively. $\tau_n$ is the time delay corresponding to the wave propagation velocity of a given medium and the distance defined as:

$$\tau_n = \frac{h_n}{V_n} \tag{4}$$

where $n$ = 1,2,3 and $h_n$ is the distance indicated in Figure 10. $V_n$ is the wave propagation velocity in the considered medium. $\tau_1$ is a time delay corresponding to the height of the building and wave propagation velocity, $V_1$ later called $V_b$, and $\tau_2$ and $\tau_3$ are related to the travel time in the soil considering the distance from the bottom of the building to the sensor, approximated as $\sqrt{h_2^2 + h_3^2}$ and the vertical uplift of the athletic field, $h_3$, and wave propagation velocity in the soil. $r$ in equation 3 is the reflection coefficient of the boundary soil-building defined as:

$$r = \frac{V_b\rho_b - V_s\rho_s}{V_b\rho_b + V_s\rho_s} \tag{5}$$

where $\rho_b$ and $\rho_s$ are the densities of the building and soil, respectively. $V_s$ is estimated as the average value of $V_2$ and $V_3$.

To estimate the time delay $\tau_1$ corresponding to the wave propagation within the structure, a simple model was developed:

$$\frac{B(\omega)}{Y(\omega)} = \frac{1}{2}e^{-i2\pi f(-\tau_1)} + \frac{1}{2}e^{-i2\pi f\tau_1} \tag{6}$$

where $B(\omega)$ is a Fourier transform of the recording registered by the sensor at the bottom of the building $b(t)$.

The model was used to estimate the travel times in the medium based on the grid search method similar to the one used by Parolai et al. (2010). The time delay search was divided into two parts. First, the time delay corresponding to the wave propagation in the building was estimated using equation 6, which later was related to the wave propagation velocity using equation 4. The second part was focused on searching the time delays in the soil, $\tau_2$ and $\tau_3$. Soil and building densities used for this study were 2350 kg/m$^3$ and 280 kg/m$^3$, respectively.

Parameters that provided minimum misfit of the model are presented in Table 2 and the comparison of the real data and best-fitting model in the time and frequency domain for the X (blue lines) and Y components (orange lines) are shown in Figure 11.

The two sensors at the largest distance from the building (921A+C and 921A+P) present a good model fit in both the time and frequency domain for the X component. The fit in the Y component is not as accurate, however, the model still defines the three main peaks of the deconvolved wavefield

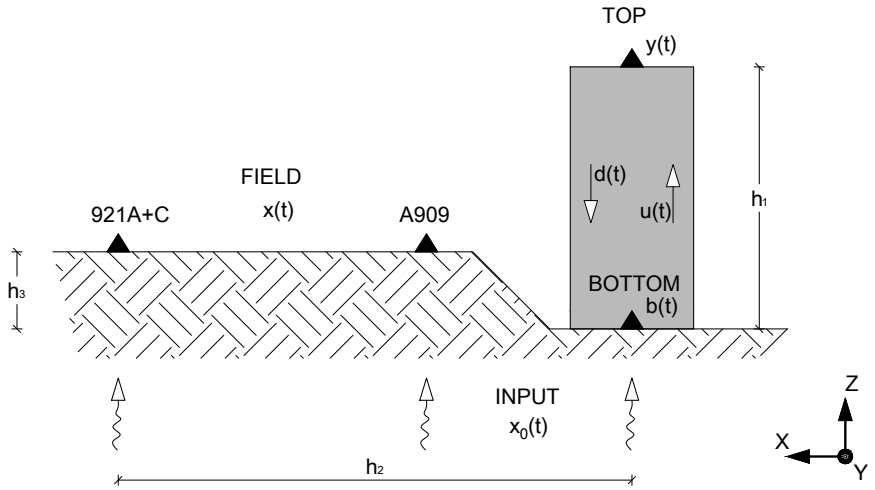


**Figure 10:** Geometry used for the analytical model. The building with height $h_1$ is indicated by the red rectangle. $h_2$ is the horizontal distance of the sensors in the field from the sensor installed at the bottom of the building, $h_3$ - is the vertical distance from the bottom of the building. $x(t)$ is the recording in the athletic field, $y(t)$ and $b(t)$ are the recordings at the top and bottom of the building, $u(t)$ and $d(t)$ - are up- and down-going waves in the building. $x_0(t)$ is the input ground motion.

| | Component | $V_b$ [m/s] | $V_2$ [m/s] | $V_3$ [m/s] |
|---|---|---|---|---|
| Array 1 | X | 262 | 133 | 203 |
| | Y | 262 | 119 | 129 |
| Array 2 | X | 253 | 132 | 137 |
| | Y | 266 | 129 | 375 |

**Table 2:** Parameters providing minimum misfit of the analytical model

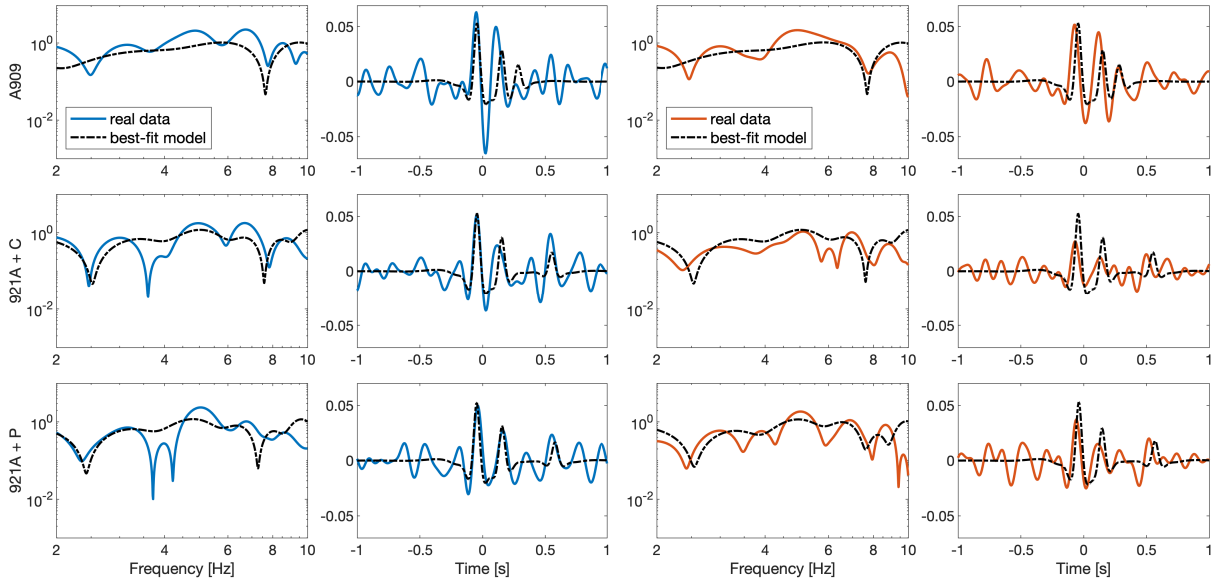


**Figure 11:** Comparison of the real data deconvolution (color lines) and analytical solution (dashed black lines). First two columns present results in frequency and time domain for the X component. The two last columns present results for the Y component.

in the time and frequency domain with satisfactory accuracy. For sensor A909 which is the closest to the structure, the model in the frequency domain is much simpler than the real data deconvolution, however in the time domain, it fits the third peak relatively accurately in both directions. Based on the analytical solution, peaks related to the parts of the wavefield transmitted from the building to the ground in the X direction are at around 0.27 s delay for sensor A909, 0.53 s for 921A+C, and 0.56s for 921A+P. In the Y direction, the identified peaks are at 0.27 s for sensor A909, 0.48 s for 921A+C, and 0.51 s for 921A+P.

## 3.5 Polarization analysis

### 3.5.1 Polarization ellipse parameters

An example of the results of the polarization ellipse parameters for sensor 921A+P in Array 2 is presented in Figure 12. In the figure, above the S spectrum of the considered parameters, the three-component trace used for the analysis is shown. In the panels below, the S spectrum of semi-major, semi-minor axis, the difference between them, and total power are in Figure 12. The time window related to the identified phases described in the previous section is indicated by gray shade in the top panel and black lines in the S spectrum plots. The four remaining ellipse parameters i.e.: inclination, the argument of max S spectrum, azimuth of ascending node, and phase, are not considered in this analysis.

In order to narrow the focus on the most energetic parts of the signal, a filter that considers only elliptical parameters' values larger than 50 % of the maximum of the total power S spectrum was used for the analysis. Based on the analysis of the S spectra of all three analyzed sensors, the distribution of the considered energy content within the selected time windows is distributed in the two frequency bands: 1 Hz - 3 Hz and 4 Hz - 8 Hz. The distribution of the three parameters defining circular and linear polarization ellipse parts from the constrained S spectrum is presented in Figure 13 with the separation for the two distinguished frequency bands.

### 3.5.2 Polarization of the reconstructed wavefield

Phases defined using the analytical model were used to reconstruct the motion in the ground related to the input motion at the top of the building. An example of the constrained deconvolution approach (after Bindi et al. (2010) applied to the Matera data is presented in Figure 14. In the top panel, the shaded area indicates the time interval used for the phase selection. In the same plot, the blue lines represent the deconvolved real data and the dashed orange line indicates the constrained wavefield. A comparison of the Fourier spectra of the two traces is presented in the middle panel with the corresponding line colors. In the bottom panel of the figure, the gray dashed lines present spectra of the original signal registered by the sensor at the top of the building, and red lines indicate the signal registered originally by the sensor in the field. The black line is the result of the convolution of the constrained Fourier spectra (orange dashed line) with the input at the top of the building (gray dashed line), which represents the reconstructed motion in the athletic field.

In the time domain, the reconstructed ground motion due to the virtual input at the top of the building is presented in Figure 15 for sensor 921A+C from Array 1 and in Figure 16 for sensor 921A+P from Array 2. The gray traces are signals originally recorded by the sensors and the black ones are the

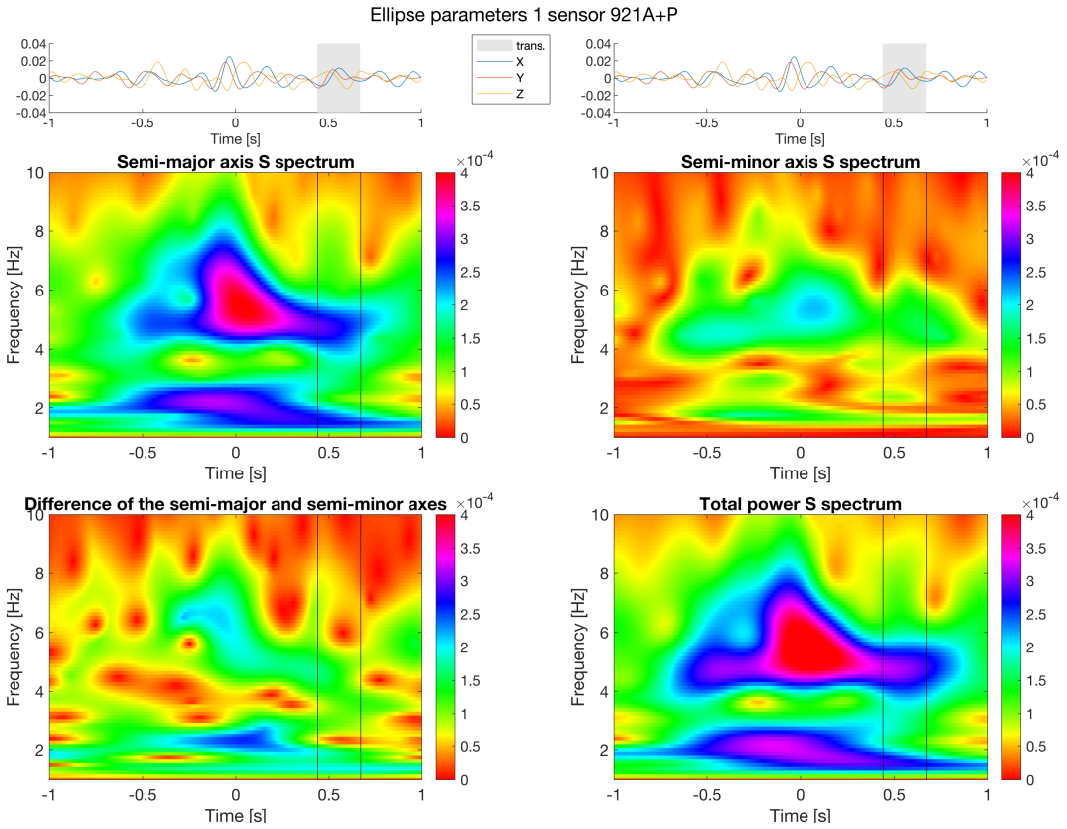


**Figure 12:** Example of the ellipse parameters results for sensor 921A+P from Array 2. On the top, are three components of the deconvolution in time used for the analysis. The gray rectangle indicates the considered time interval corresponding to the identified phases. In time-frequency plots, the same interval is marked with black thin lines.

reconstructed motion. The gray shades indicate time windows (T1, T2, and T3) for which polarization was analyzed. The color scale corresponds to the time increment of each window. Below is presented the particle motion decomposed into three planes: radial (X-Z), transverse (Y-Z), and horizontal (X-Y).

The results of both sensors show that after the decomposition of the particle motion from all chosen time windows the Z component has much smaller amplitudes than the two horizontal components. The reconstructed wavefield does not show significant particle motion in this direction. Interestingly, the elliptical trajectory is clear in the horizontal plane in all time windows. The slight difference between the two analyzed sensors is that the motion in the horizontal plane of the sensor 921A+C (Figure 15) has a higher contribution to the linear part of the ellipse than it is observed in the trajectory of the sensor 921A+P (Figure 16).

# 4 Discussion

Analysis of the data from the Matera experiment suggests that the analyzed building has complex dynamic behavior. In the data analysis using the proposed approach, exact identification of the impact of the joints between units is not necessary to obtain the results. However, the joints in the analyzed building might have an impact on the dynamic behavior of the structure, as was observed by Parolai

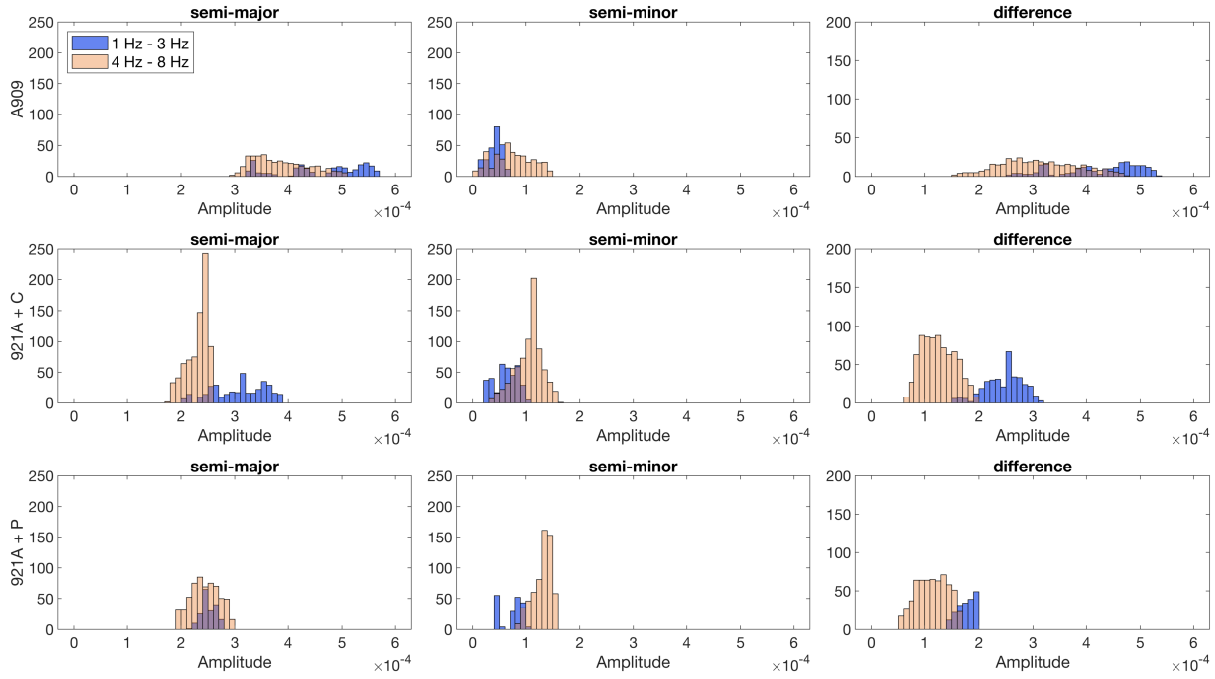


**Figure 13:** Distribution of the semi-major, semi-minor and their difference for the considered time interval related to the identified deconvolution peaks. Data is separated into two frequency bands: blue corresponds to 1 Hz - 3 Hz and orange to 4 Hz - 8 Hz.

et al. (2005) for Holweide Hospital in Germany. Despite no precise building analysis, the information about the frequency range where the majority of the structure's vibration energy is located obtained from SR analysis is sufficient for the proposed SSI assessment method.

The developed analytical model allowed better identification and interpretation of the wavefield obtained from joint deconvolution. In cases like the one in Matera, where there is a limited number of sensors in the field registering an EQ, low energy input and/or complex environmental geometry result in numerous phases in the deconvolved wavefield, the comparison of the real data results with a model is crucial. In the presented case, despite the simplified model assumptions, the fit of the model is good, both in the time and frequency domain, and it was possible to identify phases related to the energy transmitted from the building to the ground.

In the case of the Matera experiment, the combination of the joint deconvolution and polarization analysis revealed that the semi-minor axis, describing the circular part of the polarization ellipse, in the time windows of the selected phases, is significantly smaller than the difference between semi-major and semi-minor axes, which describes the linear part. Those results, especially visible in the frequency range of the dominant frequencies of the building (1 - 3 Hz), imply that the deconvolved wavefield has mostly linear polarization.

Reconstruction of the signal transmitted from the structure to the nearby athletic field and the analysis of the particle motion showed the linear behavior in radial and transverse planes. For both analyzed sensors, the vertical motion is very small and the trajectory in the horizontal plane shows significant ellipticity. In the results from the Matera experiment, the conventionally polarized Rayleigh waves, which show ellipticity in the radial plane, are not present. One possible explanation for this observation might be the unconventionally inclined Rayleigh wave or the influence of the compressional push-pull

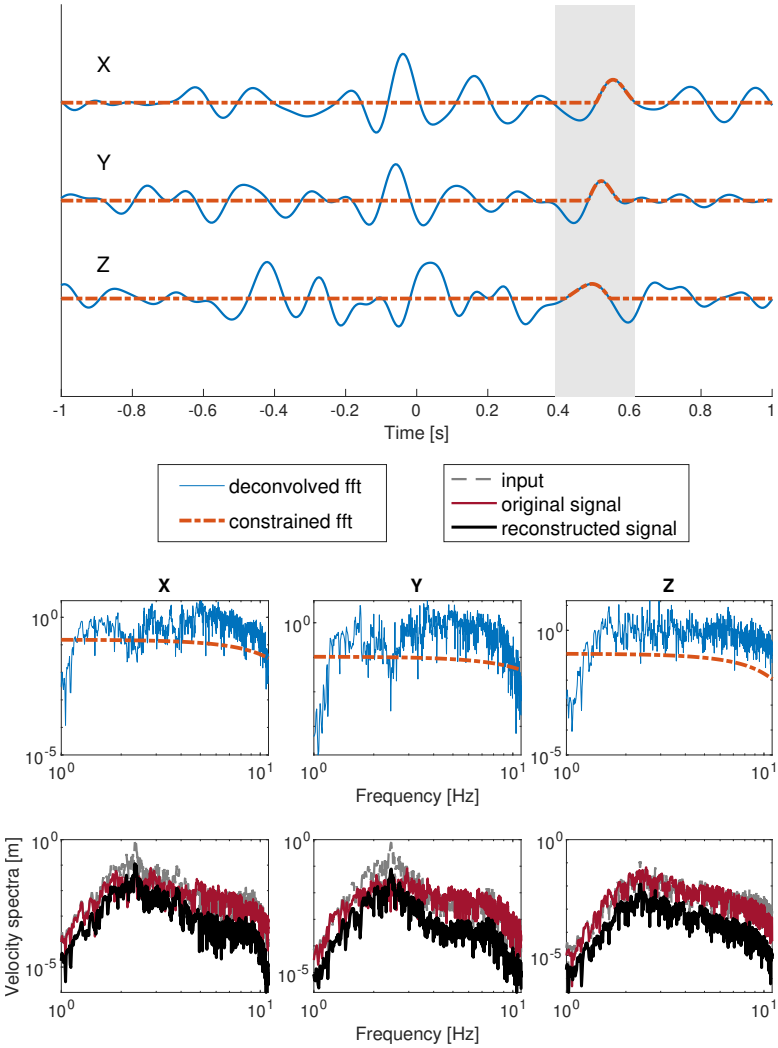


**Figure 14:** Example of the constrained deconvolution analysis for sensor 921A+P from Array 2. Top: deconvolution time history is indicated with the blue solid line. The considered time interval for constrained deconvolution is determined by gray shade. The orange dashed line indicated the constrained deconvolution in time. Middle: Fourier spectra of the time histories above with corresponding colors. Bottom: comparison of the Fourier spectra of the original signal registered by the sensor at the top of the building (gray dashed), the original signal registered by the sensor in the field (red line), and the reconstructed motion (black)

motion radiated from the building to the ground.

# 5 Summary

## 5.1 Conclusions

In this report, an innovative methodology for SSI assessment was presented. The novelty of the proposed approach is the joint analysis of the EQ data registered in the building and nearby field combining joint deconvolution based on the method of Petrovic and Parolai (2016) with the polarization analysis. Polarization analysis is a two-step process in which, firstly, the ellipse parameters of the deconvolved wavefield are analyzed using the approach proposed by Pinnegar (2006), and in the second step, using constrained deconvolution (Bindi et al., 2010), the trajectory motion is examined.

The presented methodology was tested using recordings from the Matera experiment, where a dense

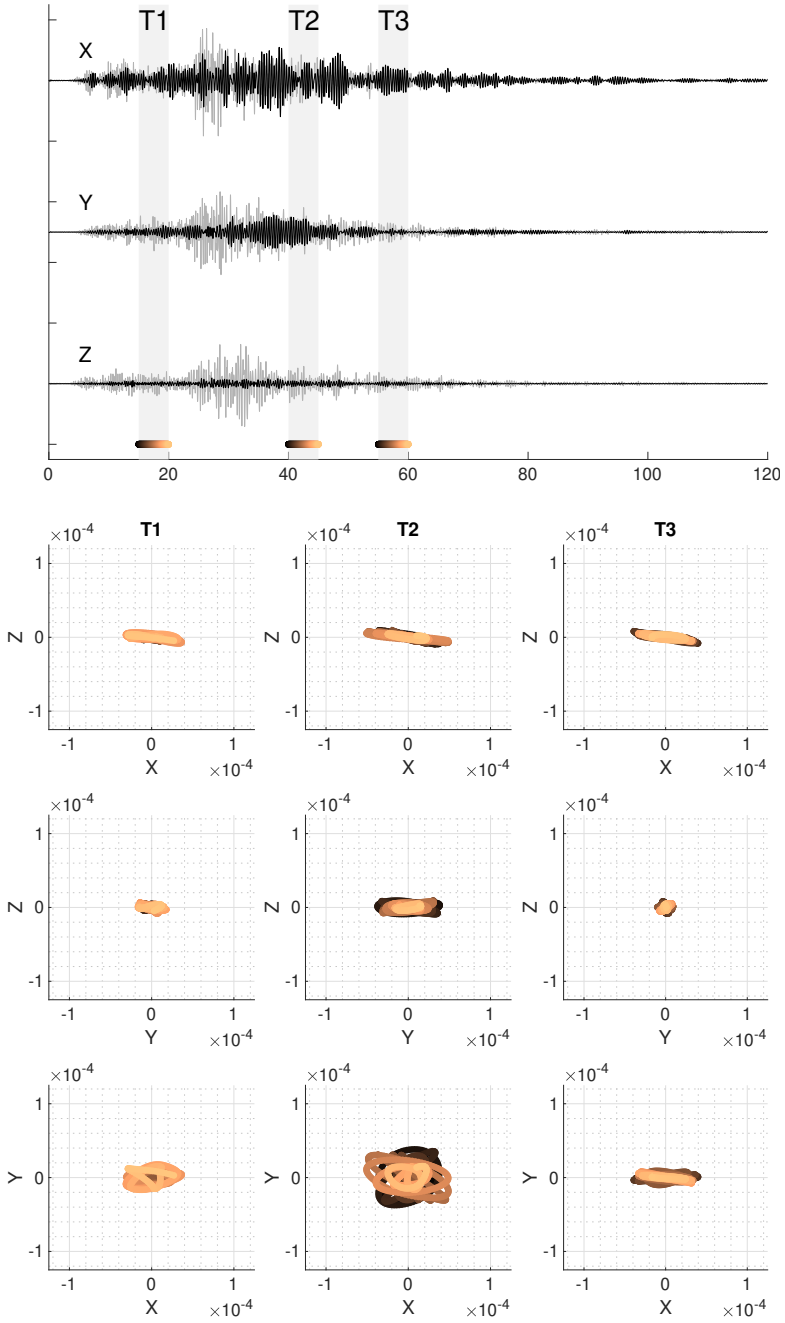


**Figure 15:** Particle motion trajectory for sensor 921A+C from Array 1. Top: time history of the originally recorded signal (gray) and the reconstructed input (black). Gray shades indicate the intervals (T1, T2, and T3) for the trajectory analysis below. Below: particle motion in three planes - radial (X-Z) in the first row, transverse (Y-Z) in the middle row, and horizontal (X-Y) in the bottom. The color scale of the trajectory plots corresponds to the increment of time (from blue to yellow) indicated at the bottom of the time history plots.

array of sensors was installed both in the building and on the nearby athletic field. Polarization analysis revealed that the wavefield presumably radiated from the building to the ground has mostly linear polarization. The decomposed particle motion analysis showed that both in radial and transverse planes, the trajectory is mostly linear. Elliptical motion is observed only in the horizontal plane. The proposed new methodology for SSI assessment allows an estimation of the polarization of the wavefield transmitted to the ground. This knowledge provides information for the characterization of the wavefield, which could be of great importance for further analysis of the structures' interaction during ground shaking. Therefore, this methodology could be potentially used to mitigate the negative

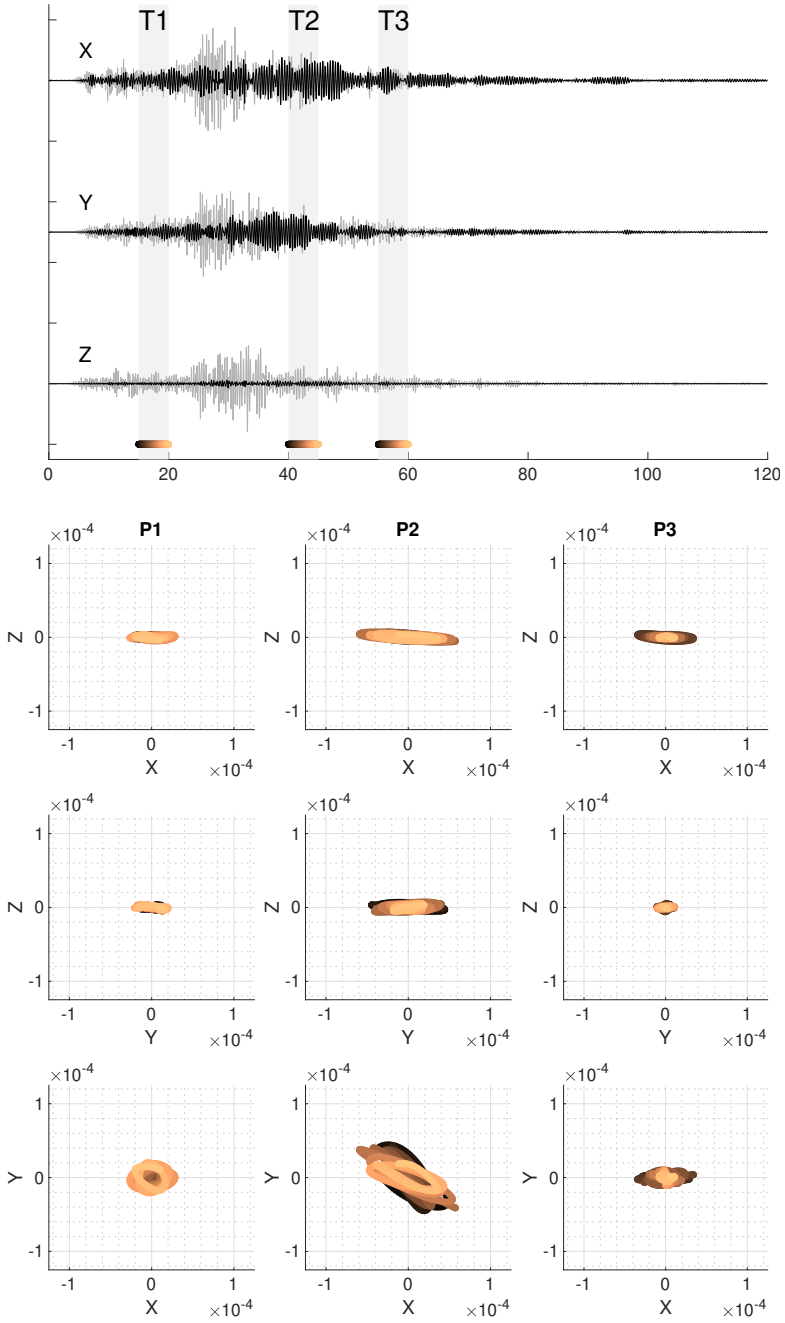


**Figure 16:** Same as Figure 15 but for sensor 921A+P from Array 2.

influence of moderate to strong motion in urban areas.

## 5.2 Outlook

The proposed innovative methodology for soil-structure interaction assessment is a part of an ongoing research project focused on this subject. The following approach is based on the analysis of the earthquake recording, but in further steps, the extension of the methodology to noise analysis is planned. Validation of the methodology using numerical modeling is currently under preparation. Additionally, a second SSI experiment, in a controlled environment and with simplified geometry is planned, to obtain a second data set for the validation of the proposed approach.

## References


Astorga, A., Guéguen, P., and Kashima, T. (2018). Nonlinear elasticity observed in buildings during a long sequence of earthquakes. *Bulletin of the Seismological Society of America*, 108(3):1185–1198.

Bindi, D., Parolai, S., Picozzi, M., and Ansal, A. (2010). Seismic input motion determined from a surface-downhole pair of sensors: A constrained deconvolution approach. *Bulletin of the Seismological Society of America*, 100(3):1375–1380.

Cardenas, M., Bard, P.-Y., Guèguen, P., and Chavez-Garcia, F. J. (2000). Soil-structure interaction in mexico city. wave field radiated away from jalapa building: Data and modelling. In *Proc. of the 12th World Conference on Earthquake Engineering*. 12 WCEE 2000, Auckland, New Zeland. Paper No. 385.

Chandra, J. and Guèguen, P. (2019). Nonlinear response of soil–structure systems using dynamic centrifuge experiments. *Journal of Earthquake Engineering*, 23(10):1719–1741.

CLARA project (2020). Clara WebGIS. `https://smartcities-matera-clara.imaa.cnr.it/`.

Clayton, R. W. and Wiggins, R. A. (1976). Source shape estimation and deconvolution of teleseismic bodywaves. *Geophysical Journal International*, 47(1):151–177.

Fares, R., Santisi d'Avila, M. P., and Deschamps, A. (2019). Soil-structure interaction analysis using a 1DT-3C wave propagation model. *Soil Dynamics and Earthquake Engineering*, 120(February):200–213.

Gallipoli, M. and Lupo, M. (2012). Caratterizzazione dei terreni e risposta sismica locale dell'area urbana di Matera. Tecniche speditive per la stima dell'amplificazione sis- mica e della dinamica degli edifici Studi teorici ed applicazioni professionali a cura di Marco Mucciarelli (In Italian). *ARACNE editrice S.r.l.*, page 323–342.

Guèguen, P. and Bard, P.-Y. (2005). Soil-structure and soil-structure-soil interaction: Experimental evidence at the volvi test site. *Journal of Earthquake Engineering*, 9(5):657–693.

Guèguen, P., Bard, P.-Y., and Chavez-Garcia, F. J. (2002). Site-city seismic interaction in mexico city–like environments: An analytical study. *Bulletin of the Seismological Society of America*, 92(2):794–811.

Guéguen, P. and Colombi, A. (2016). Experimental and numerical evidence of the clustering effect of structures on their response during an earthquake: A case study of three identical towers in the City of Grenoble, France. *Bulletin of the Seismological Society of America*, 106(6):2855–2864.

Isbiliroglu, Y. D., Taborda, R., and Bielak, J. (2013). Coupled soil-structure interaction effects of building clusters during earthquakes. *Earthquake Spectra*, 31(1):463–500.

Jennings, P. C. (1970). Distant motions from a building vibration test. *Bulletin of the Seismological Society of America*, 60(6):2037–2043.

Kausel, E. (2010). Early history of soil-structure interaction. *Soil Dynamics and Earthquake Engineering*, 30(9):822–832.

Kham, M., Semblat, J.-F., Bard, P.-Y., and Dangla, P. (2006). Seismic Site–City Interaction: Main Governing Phenomena through Simplified Numerical Models. *Bulletin of the Seismological Society of America*, 96(5):1934–1951.

Kumar, N. and Narayan, J. P. (2017). Quantification of site–city interaction effects on the response of structure under double resonance condition. *Geophysical Journal International*, 212(1):422–441.

Liang, J., Fu, J., Todorovska, M. I., and Trifunac, M. D. (2013). Effects of the site dynamic characteristics on soil–structure interaction (i): Incident sh-waves. *Soil Dynamics and Earthquake Engineering*, 44:27–37.

Massa, M., Marzorati, S., Ladina, C., and Lovati, S. (2010). Urban seismic stations: Soil-structure interaction assessment by spectral ratio analyses. *Bulletin of Earthquake Engineering*, 8(3):723–738.

Paolucci, R. (1993). Soil-structure interaction effects on an instrumented building in Mexico City. *European Earthquake Engineering*, 3:33–44.

Parolai, S., Bindi, D., Ansal, A., Kurtulus, A., Strollo, A., and Zschau, J. (2010). Determination of shallow S-wave attenuation by down-hole waveform deconvolution: A case study in Istanbul (Turkey). *Geophysical Journal International*, 181(2):1147–1158.

Parolai, S., Fäcke, A., Richwalski, S. M., and Stempniwski, L. (2005). Assessing the Vibrational Frequencies of the Holweide Hospital in the City of Cologne (Germany) by Means of Ambient Seismic Noise Analysis and FE modelling. *Natural Hazards*, 34(2):217–230.

Petrovic, B. and Parolai, S. (2016). Joint deconvolution of building and downhole strong-motion recordings: Evidence for the seismic wavefield being radiated back into the shallow geological layers. *Bulletin of the Seismological Society of America*, 106(4):1720–1732.

Petrovic, B., Parolai, S., Pianese, G., Dikmen, S. U., Moldobekov, B., Orunbaev, S., and Paolucci, R. (2018). Joint deconvolution of building and downhole seismic recordings: an application to three test cases. *Bulletin of Earthquake Engineering*, 16(2):613–641.

Petrovic, B., Parolai, S., Romanelli, M., Affatato, A., Petronio, L., Barbagallo, A., Sorgo, D., Stefani, M., and Caputo, R. (2019). Un approccio innovativo per una migliore comprensione dell'interazione sismica tra suolo e strutture: Il test site di ferrara. *Bollettino di Geofisica Teorica ed Applicata*, 60(2):140–147.

Pinnegar, C. R. (2006). Polarization analysis and polarization filtering of three-component signals with the time–frequency s transform. *Geophysical Journal International*, 165(2):596–606.

Pitilakis, D., Dietz, M., Wood, D. M., Clouteau, D., and Modaressi, A. (2008). Numerical simulation of dynamic soil–structure interaction in shaking table testing. *Soil Dynamics and Earthquake Engineering*, 28(6):453–467.

Skłodowska, A. M., Holden, C., Guéguen, P., Finnegan, J. P., and Sidwell, G. (2021). Structural change detection applying long-term seismic interferometry by deconvolution method to a modern civil engineering structure (new zealand). *Bulletin of Earthquake Engineering*, 19:3551 – 3569.

Snieder, R. (2009). Extracting the time-domain building response from random vibrations. In Schanz,

T. and Iankov, R., editors, *Coupled site and soil-structure interaction effects with application to seismic risk mitigation*, pages 283–292. Springer, Dordrecht.

Snieder, R. and Şafak, E. (2006). Extracting the Building Response Using Seismic Interferometry: Theory and Application to the Millikan Library in Pasadena, California. *Bulletin of the Seismological Society of America*, 96(2):586–598.

Stockwell, R. G., Mansinha, L., and Lowe, R. P. (1996). Localization of the complex spectrum: the s transform. *IEEE Transactions on Signal Processing*, 44(4):998–1001.

Todorovska, M. I. (2009). Seismic interferometry of a soil-structure interaction model with coupled horizontal and rocking response. *Bulletin of the Seismological Society of America*, 99(2 A):611–625.

Vidale, J. E. (1986). Complex polarization analysis of particle motion. *Bulletin of the Seismological Society of America*, 76(5):1393–1405.

Wirgin, A. and Bard, P.-Y. (1996). Effects of buildings on the duration and amplitude of ground motion in Mexico City. *Bulletin of the Seismological Society of America*, 86(3):914–920.

Yoshida, K. and Sasatani, T. (2008). Seismic vertical array analysis for phase decomposition. *Geophysical Journal International*, 174(2):707–718.